Journal of Catalysis 374 (2019) 43–50

Contents lists available at ScienceDirect

Journal of Catalysis

journal homepage: www.elsevier.com/locate/jcat

Incorporation of CeF_3 on single-atom dispersed Fe/N/C with oxophilic interface as highly durable electrocatalyst for proton exchange membrane fuel cell

Xue Yin [a], Wellars Utetiwabo [a], Shuhui Sun [b], Yimeng Lian [a], Renjie Chen [c], Wen Yang [a,*]

[a] Key Laboratory of Cluster Science of Ministry of Education, Beijing Key Laboratory of Photoelectronic/Electrophotonic Conversion Materials, School of Chemistry and Chemical Engineering, Beijing Institute of Technology, Beijing 100081, PR China
[b] Institut National de la Recherche Scientifique – Énergie Matériaux et Télécommunications, 1650 Boulevard Lionel-Boulet, Varennes, Quebec J3X 1S2, Canada
[c] School of Material Science and Engineering, Beijing Institute of Technology, Beijing 100081, PR China

ARTICLE INFO

Article history:
Received 21 January 2019
Revised 29 March 2019
Accepted 16 April 2019
Available online 3 May 2019

Keywords:
Oxophilic interface
Ce^{3+} sites
CeF_3-Fe/N/C hybrid catalyst
Oxygen reduction reaction
Durability

ABSTRACT

Herein, we demonstrate a bottom-up synthetic method resulting in a nanocomposite which consist of cerium fluoride (CeF_3) embedded in iron-nitrogen-doped porous carbon (Fe/N/C) utilizing fluorination and ammonia annealing. High-angle annular dark field scanning transmission electron microscopy (HAADF-STEM) combined with X-ray absorption spectroscopy (XAS) verifies that the Fe species are present as Fe-N_4 coordination at an atomic level in the CeF_3-Fe/N/C catalyst. A high-spin Fe^{3+}-N_4 configuration in the nitrogen-doped carbon revealed by ^{57}Fe Mössbauer spectrum and X-ray absorption spectroscopy for Fe *L*-edge, which will contribute to the oxygen reduction reaction (ORR) activity in acid electrolyte. CeF_3 embedded into the structure of Fe/N/C not only form the oxophilic interface, but also regulate the surface chemical state of Fe and Ce species as well as boosting ORR in acidic solution. The presence of Ce^{3+} sites at the CeF_3-Fe/N/C hybrid catalyst could enhance the O_2 adsorption capability and promote H_2O_2 reducing to water efficiently, thus greatly improve of the electrochemical performance and durability of Fe/N/C catalyst is demonstrated in proton exchange membrane fuel cell (PEMFC).

1. Introduction

The electrochemical oxygen reduction reaction (ORR) has attracted much interest due to its application in polymer electrolyte membrane fuel cells (PEMFC), and the noble metal Pt-based materials are regarded as efficient electrocatalysts for ORR [1,2]. For the large-scale applications of PEMFC, a low-cost electrocatalyst alternative to Pt for the ORR is imperative [3,4]. The atomically dispersed iron-nitrogen-carbon (Fe/N/C) catalysts have been considered as the most promising candidates to replace the Pt-based ORR catalysts [5–7]. Nevertheless, the ORR activity catalyzed by Fe/N/C catalyst is sluggish in an acidic electrolyte, which leads to relatively high overpotential (40–400 mV) and remarkable performance loss in PEMFC [8,9]. The overpotential is related to the proton and electron transfer to the adsorbed oxygen on the surface of catalysts [10,11]. One of the effective strategies to address those issues is to promote high-concentration oxygen to react with the reactive catalytic sites [9]. Some studies purpose the interface for ORR at the triple phase among the electrolyte, gas phase and reactive catalytic sites. There is a feature of high oxygen solubility and fast electron transport at the interface, where the oxygen reduction takes place [12]. Consequently, it is highly desirable to design the interface at reactive catalytic sites which can promote the electron transport as well as enhancing the reactant oxygen to accelerate the reaction. Meanwhile, the Fe/N/C catalyst in PEMFC often degrades rapidly in short term [13,14], it is believed that the by-product H_2O_2 will generate highly reactive oxygen-containing radicals in the presence of free iron species, and then lead to the degradation of Fe/N/C catalyst [15,16]. Therefore, it is possible to achieve the high stability of Fe/N/C catalyst by enhancement of oxygen adsorption capacity and the elimination of H_2O_2 production.

Ce^{3+}/Ce^{4+} redox couple in CeO_2 are well known for its high oxygen mobility, oxygen storage capacity [17–19], efficient absorption of H_2O_2 and scavenging of free radicals [20,21]. Recent studies indicated that the elimination of H_2O_2 is correlated to the fraction of Ce^{3+} species in CeO_2, and latter always used as co-catalyst or supporter in the metals-based hybrid electrocatalyst for ORR [22,23]. Another promising cerium-containing material is CeF_3, which also

---

[*] Corresponding author.
E-mail address: wenyang@bit.edu.cn (W. Yang).

https://doi.org/10.1016/j.jcat.2019.04.028
0021-9517/

has Ce^{3+}/Ce^{4+} dynamic redox couple, showing structural stability in an acidic environment, as well as high ionic conductive and intriguing catalytic properties [24–26]. More importantly, CeF_3 is the most studied cerium (III) compounds, while the Ce^{4+} can be formed only as a result of non-stoichiometry [27]. To the best of our knowledge, there are no studies related to the application of metal fluoride (CeF_3) as co-catalyst to enhance the ORR durability of Fe/N/C catalyst in the PEMFC due to limited synthetic methods for preparation of metal fluoride.

In this work, to address these challenges and realize potential application in PEMFC, we report a bottom-up synthetic strategy to prepare the metal fluoride/single iron atom (CeF_3-Fe/N/C) hybrid catalyst. We discovered that the CeO_2 nanoparticles preconfined in iron-nitrogen-doped porous carbon catalyst can be facilely transformed to CeF_3, by reacting with fluoride agent at room temperature and subsequent heat treatment with NH_3. Though this synthetic strategy, the CeF_3 is anchored on the structure of Fe/N/C and formed the interface in CeF_3-Fe/N/C hybrid catalyst. At the same time, the surface chemical state of Fe and Ce species could be regulated due to the strongly chemical interaction between CeF_3 and Fe/N/C. O_2 temperature programmed desorption/mass spectrometry illustrated that the oxophilic interface play an important role in the O_2 adsorption capacity increased with the introduction of CeF_3. The ORR catalyzed by CeF_3-Fe/N/C mainly happens through 4-electron pathway, and the hybrid catalyst could adsorb and convert H_2O_2 to water effectively by ex-situ chemical treatment of catalysts with H_2O_2. Thus, excellent electrochemical performance and stability for ORR in PEMFC was achieved in this work.

2. Experimental section

2.1. Synthesis of the catalysis

2.1.1. Synthesis of the CeO_2 nanoparticles [28]

Briefly, an aqueous urea solution (0.1 g mL^{-1}) was added to 0.1 M $Ce(NO_3)_3{\cdot}6H_2O$ aqueous solution. The suspension was stirred at 80 °C for 12 h, followed by heat-treatment at 550 °C for two hours.

2.1.2. Synthesis of the CeF_3-Fe/N/C hybrid catalyst [29,30]

To confine active material into the pores with high dispersibility, the as-synthesized CeO_2 was ultrasonically dispersed in an aqueous solution containing 5 g SiO_2 and 0.25 g PEI to form a homogenous solution. Aniline (2 g) and an amount of iron (II) phthalocyanine (FePc) was gradually added to 20 ml HCl (2 M) solution to form a suspension. Then, 2 g ammonium persulphate ($N_2H_8S_2O_8$) was added to the suspension. The polymerization of aniline was completed after reaction for 24 h, the suspension was vacuum-dried, and then carbonized in a tube furnace at 900 °C for one hour under nitrogen. The obtained powder was etched with a 4 M HF solution for 24 h at room temperature to remove the SiO_2 template and fluorination of CeO_2, then washed several times with deionized water. Subsequently, the obtained solids were pyrolyzed in an NH_3 atmosphere at 900 °C (the synthesis route is illustrated in Scheme S1). For comparison, series of CeF_3-Fe/N/C composites were prepared by the same procedure for comparison, with the different amount of cerium fluoride (0%, 2.5%, 5%, 7.5% and 10%).

2.1.3. Ex-suit chemical treatment of the catalyst with hydrogen peroxide [15]

A 50 mg sample was dispersed and stirred in 0.1 M H_2O_2 solution heated to 80 °C under reflux. Once the H_2O_2 had been added, the solution was stirred for 24 h at 80 °C, and then the catalyst powder was washed with water before overnight drying at 60 °C.

2.2. Structural analysis

X-ray diffraction (XRD) was used to characterize the lattice structure of these samples. The Fourier transform infrared spectroscopy (FTIR) was obtained using a Perkin–Elmer instrument. X-ray photoelectron spectroscopy (XPS) data was recorded on a Thermo ESCALAB 250XI instrument with a monochromatized Al, Ka X-ray source. The morphology and elemental distribution of the samples were observed using the transmission electron microscope (TEM) and high resolution transmission electron microscope (HRTEM). The high-angle annular dark-field scanning transmission electron microscopy (HAADF-STEM) images were performed on a JEOL JEM-2100F fieldemission transmission electron microscope. The metal content was analyzed by inductively coupled plasma-atomic emission spectroscopy (ICP-OES). ^{57}Fe Mössbauer spectra was measured at room temperature using a Topologic 500A spectrometer and a proportional counter. X-ray absorption spectroscopy was measured at Beijing Synchrotron Radiation Facility. O_2-TPD/MS (O_2-temperature programmed desorption mass spectrometry) measurements were performed on an AutoChem 2910 chemisorption analyzer. All samples were first treated at 200 °C for 30 min under an Ar atmosphere to remove adsorbed water. Then, after the samples had cooled to room temperature, an O_2/Ar gas flow of 30 sccm was introduced to adsorb on the samples for one hour. After the remaining O_2 was evacuated using a He gas flow, the temperature of the samples was raised at a rate of 20 °C min^{-1} from room temperature to 800 °C. The effluents were monitored by an e-Vision + residual gas analyzer MKS coupled with a quadrupole mass selective detector.

2.3. Electrochemical measurements

Rotating disk electrode (RDE) and rotating ring-disk electrode (RRDE) tests were carried out on a CHI760D workstation (Shanghai Chenhua, China) at room temperature. A graphite rod and an Ag/AgCl electrode were used as the counter and reference electrodes, respectively. RDE tests were conducted in an oxygen saturated 0.5 M H_2SO_4 electrolyte and a glassy carbon work electrode (4 mm of disk outer diameter) with the rotating rate varying from 400 to 2500 rpm at a scan rate of 5 mV s^{-1}. The catalyst ink was prepared by adding a 5 mg catalyst to a solution containing 280 μL water, 70 μL ethanol and 95 μL Nafion (5 wt%) to form a homogeneous suspension. Then 8 μL of ink was dropped onto the glassy carbon disk. For comparison, a commercial 20% Pt/C was used. Koutecky–Levich plots (j^{-1} vs. $\omega^{-1/2}$) were analyzed in 0.5 M H_2SO_4 with varying rotation speeds. For the long-term stability tests, the electrodes were first cycled 3000 cycles from 0.4 V to 1.0 V at 50 mV s^{-1} in 0.5 M H_2SO_4. In addition, RRDE tests were carried out with a three-electrode system similar to that of RDE tests except for the working electrode. The work electrode contains glassy carbon disk (OD = 4 mm) and platinum ring (OD = 7 mm, ID = 5 mm). The RRDE tests of different catalysts were performed in the saturated 0.5 M H_2SO_4 electrolyte, the hydrogen peroxide yield and the electron-transfer number (n) of different catalysts during the ORR was detected by using Pt ring electrode that ring potential was constant at 1.1 V versus RHE.

3. Results and discussion

3.1. Structural characterization of catalysts

XRD was used to identify the crystalline structures of Fe/N/C, CeF_3-Fe/N/C and CeF_3-N/C. It can be seen from Fig. 1a that two broad diffraction peaks of about 24° and 44° in Fe/N/C, which are assigned to (0 0 2) and (1 0 1) diffraction of the graphitic carbon,

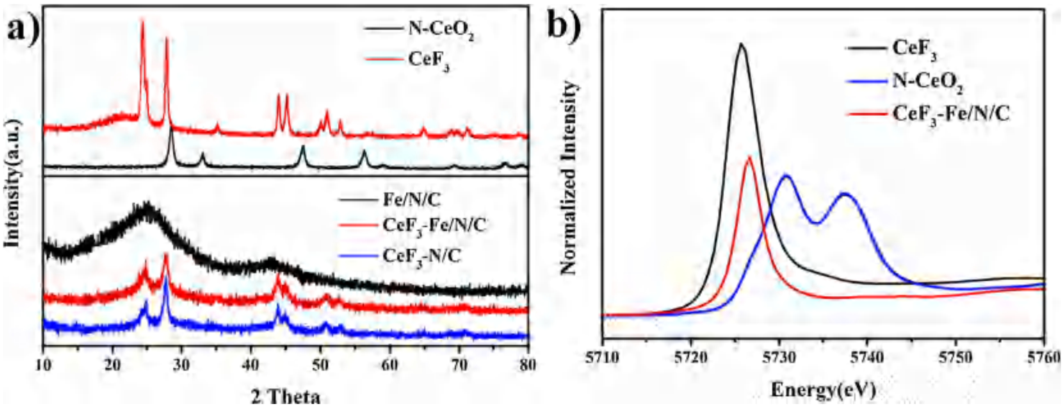

Fig. 1. (a) XRD patterns of Fe/N/C, CeF_3-Fe/N/C and CeF_3-N/C. (b) XANES spectra at Ce L_3-edge of CeF_3, N-CeO_2 and CeF_3-Fe/N/C.

respectively [31]. Due to the overlapping of CeF_3 (average 16 nm), these peaks disappear in the CeF_3-Fe/N/C and CeF_3-N/C. The six additional peaks corresponding to the CeF_3 phase (PDF#: 08-0045) can be observed, which confirmed the presence of CeF_3. Moreover, the absence of crystalline iron species peaks suggesting that Fe is consist in the Fe-N_x coordination or the content is lower than the detection limit, since the ICP analysis (The content of Fe in the Fe/N/C and CeF_3-Fe/N/C catalysts is 0.47 wt% and 0.41 wt%) confirmed the existence of Fe. The FTIR spectrum (Fig. S2) of CeF_3-Fe/N/C shows a new absorption peak at about 500 cm^{-1}, which corresponds to the stretching vibration of Ce—F bond [24], indicating the successful doping of CeF_3 into the Fe/N/C. The surface composition was examined by XPS (Fig. S3), where the typical signals for carbon, nitrogen, oxygen, fluorine and cerium were observed. And the content of Ce in CeF_3-Fe/N/C is 6.8% by ICP analysis. These results demonstrate that the CeF_3 has been doped into the structure of Fe/N/C. The X-ray absorption near-edge structure (XANES) spectra was used to get more insight into the oxidation state of Ce in CeF_3-Fe/N/C (Fig. 1b). Two distinct peaks corresponding to Ce^{4+} are observed at 5732 and 5738 eV for pure N-CeO_2 powder, while a strong single peak at 5725 eV is attributed to 2p → 5d transition in pure CeF_3 powder [32]. The Ce L_3 edge XANES spectra of CeF_3-Fe/N/C showed one characteristic peak and it is similar to that of pure CeF_3, clarifying the valence state of Ce as +3 state in the doped sample.

The morphology and structures of the as-prepared samples were characterized by TEM. Fig. 2a and b reveal that CeF_3 crystals are distributed at the surface of CeF_3-Fe/N/C sample, which is consistent with the XRD result. Additionally, the samples display many pores with a diverse size in the carbon matrix, which agree with N_2 adsorption-desorption isotherms and the pore size distribution (Fig S4 and Table S1). Noticably the larger surface area and more mesopore structure of CeF_3-Fe/N/C can expose more active sites and facilitate the transfer of reactive species (protons and reactant gases), therefore improving the catalytic performance [33,34]. HRTEM was employed to confirm the CeF_3 with intimate contact on the porous carbon framework (Fig. 2c). Flake-like nanocrystals exhibiting lattice fringes with a spacing of ca. 0.31 nm from the (1 1 1) planes of CeF_3 are observed [27]. It can be seen that the nanocrystals embedded in the carbon layer, and an irregular borderline appear in the disordered region (marked by the red line), indicating the formation of a heterostructure interface state between CeF_3 nanocrystals and the carbon layer. The Fe species were suspected to exist in the formation of Fe-N_x coordination, but such nitrogen-coordinated atomic Fe sites were never directly observed yet. Here, atomic level HAADF-STEM images provided a direct evidence, a typical region of CeF_3 was selected to observe the surface (Fig. 2d). The lattice fringes correspond to the CeF_3 (1 1 1) planes and the bright-dot contrast in HAADF-STEM images presents the position of Fe atoms. Also, isolated and well-dispersed Fe atomic sites were directly observed in the CeF_3-Fe/N/C (some Fe single atoms were circled in red for better observation in Fig. 2e), which were both located at edge sites and embedded in the carbon matrix. Therefore, the form of iron in the catalyst is atomic single sites, which are dispersed on both the carbon layer and the CeF_3. X-ray elemental mapping (Fig. 2f) further verifies that Ce and Fe species are homogeneously distributed over the CeF_3-Fe/N/C architecture (the Fe/N/C sample in Fig. S5). In addition, a uniform distribution of N and F species across the structure, clarifying that CeF_3 is encapsulated in an N-doped thin carbon layer.

To explore the inherent structure of iron subnano species at atomic level, we conducted X-ray absorption structure (XAS) and Mössbauer spectroscopy to study the chemical state and local environment of atom Fe. Fig. 3a represents Fourier transformed Fe *K*-edge EXAFS (extended X-ray absorption fine spectra, Fe *K*-edge spectra in Fig. S6) for the prepared samples, the visible peak at 1.44 Å indicates the existence of a large amount of Fe—N coordination [5] in Fe/N/C and CeF_3-Fe/N/C. In addition, compared to Fe foil and Fe_2O_3, the absence of a significant peak at around 2.2 Å for the Fe—Fe coordination indicated that the Fe species are atomically dispersed, which is consistent with the HAADF-STEM results. As shown in Fig. 3b, the electronic structure of Fe was analyzed by Fe *L*-edge XANES. The *L*-edge absorption spectrum is sensitive to the valence and spin states of the measured elements [35]. The L_3 edge ranges from 708 eV to 714 eV and involves transitions from Fe $2p_{3/2}$ to 3d states, and the L_2 edge (722–728 eV) involves transition from Fe $2p_{1/2}$ to 3d states [36]. The Fe *L*-edge of Fe/N/C exhibits only a broad peak at 712 eV attributed to Fe^{3+}. However, the CeF_3-Fe/N/C shows two split peaks at 709.7 and 712 eV, assigned to Fe^{2+} and Fe^{3+}. This phenomenon indicates that Fe^{3+} is dominant in Fe/N/C and CeF_3-Fe/N/C, and formed part of Fe^{2+} due to the electron interaction between Fe atoms and CeF_3. Furthermore, the area ratio of L_3/L_2 [37] in the samples (the L_3/L_2 ratio for Fe/N/C is 3.95 and CeF_3-Fe/N/C is 2.1) suggest that Fe^{3+} in a high spin state, implying the predominant Fe^{3+}-N_4 high spin state in Fe/N/C and CeF_3-Fe/N/C. Mössbauer spectra was used to distinguish different Fe species, and parameters are listed in Table S2. Two groups of double peaks fitted with D1 and D2 components are observed in CeF_3-Fe/N/C (Fig. S7) and Fe/N/C (Fig. S8). The absence of singlet or sextet peaks indicates that there is no any other Fe-related phase and all of Fe exist as the Fe—N species in samples [38,39]. The doublet D1 is commonly assigned to the low-spin state of ferrous in the square-planar Fe-N_4 coordination structure, and the D2 is assigned to the Fe^{3+}-N_4 high spin state. According to the previous reports, the doublet D2 is recognized as active site for the ORR [5,37]. Most of Fe exists as high spin Fe^{3+}-N_4 configuration in our catalysts, fur-

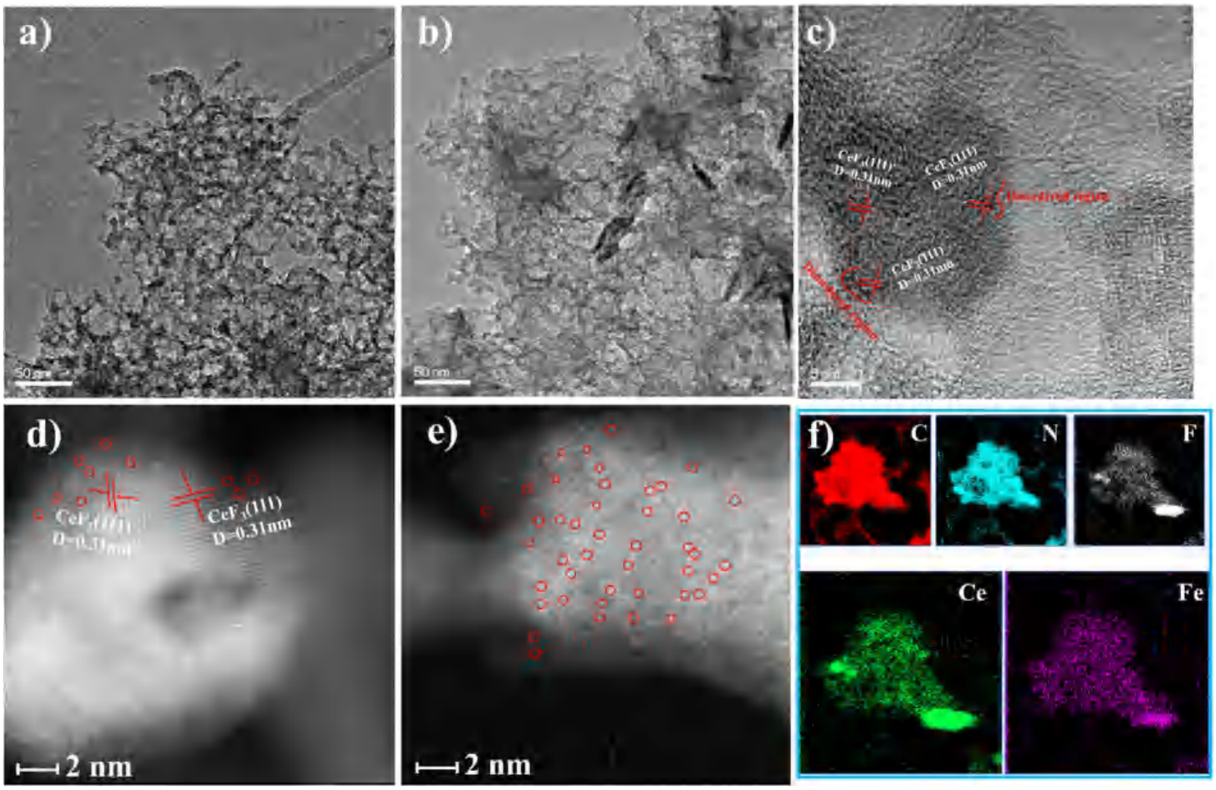

Fig. 2. TEM images of (a) Fe/N/C. (b) CeF_3-Fe/N/C. (c) HRTEM image of CeF_3-Fe/N/C. (d) HAADF-STEM image of CeF_3 and single Fe atoms (highlighted by red circles). (e) HAADF-STEM image of the CeF_3-Fe/N/C. Single Fe atoms highlighted by red circles. (f) EDS mapping of CeF_3-Fe/N/C.

ther quantitative analysis revealed that the content of D2 is 0.27 wt% and 0.25 wt% in Fe/N/C and CeF_3-Fe/N/C.

Because of the fact that the interface between CeF_3 nanocrystals and carbon layer was observed, we carried out C *K*-edge and N *K*-edge XANES to study the chemistry and electronic structure of these samples to find out if the CeF_3 in Fe/N/C changes the carbon matrix structure. The pre-edge regions are set to zero and the spectra are normalized to their total integrated intensities. Two main peaks at 285.9 eV (C—C π^* resonance) and 292.7 eV (C—C σ^* resonance) [40] are displayed in C *K*-edge XANES spectra (Fig. 3a). Compared with the σ^* peak of Fe/N/C, the intensity of CeF_3-Fe/N/C is relatively low due to the damage of the sp^2 carbon crystallinity by the CeF_3. The intensity of the π^* peak is decreased after introduction CeF_3 to Fe/N/C, further indicating that charge is transferred from CeF_3 to the π-conjugated systems of the aromatic ring in the Fe/N/C structure [35,41]. The weak peak at around 288.8 eV is related to C—N bond, since this feature is visible in the same position as that in N/C (Fig. S9). The N *K*-edge spectra (Fig. S10) of the samples exhibit three main peaks at 399.6, 402.3 and 408.3 eV, which can be related to π^* transition to pyridinic, pyrrolic states and C—N σ^* transition [42]. We find that the intensity of each peak increased for CeF_3-Fe/N/C hybrid catalyst, clarifying an electronic interaction between CeF_3 and N-group owing to partial electron transfer from N-group to Ce^{3+} ion [41]. Furthermore, XANES spectra at the Ce L_3 edge (Fig. 1b) of CeF_3-Fe/N/C showed one characteristic peak at 5726 eV, which correspond to the state of Ce^{3+}. In comparison to pure CeF_3 (the characteristic peak at 5725 eV), the feature peak of CeF_3-Fe/N/C shifted to higher energy, which unequivocally corroborates the charges were transferred from CeF_3 to Fe/N/C [11,32,43]. Thus, the surface chemical state was regulated by the Ce^{3+} sites due to the chemical interaction between CeF_3 and Fe/N/C.

It has been reported that the existence of Ce^{3+} sites could promote the release/storage of more oxygen for oxygen reduction [19,44]. O_2-TPD/MS tests were executed to investigate the O_2 adsorption ability of the catalysts (Fig. 3d). In general, the desorption peaks at low temperature (<200 °C) are ascribed to physically adsorbed O_2 species weakly connected to the surface, which are easily desorbed. The desorption peaks below 500 °C correspond to chemically adsorbed oxygen on the surface [45]. The O_2-TPD curves of Fe/N/C and CeF_3-Fe/N/C exhibit three distinct peaks at similar desorption regions (200–500 °C), indicating the presence of chemically adsorbed oxygen in both catalysts. The desorption peaks of CeF_3-Fe/N/C show a slight negative shift, suggesting that the existence of Ce^{3+} sites reduces the desorption energy barrier of oxygen [4]. Moreover, the desorption peak area of CeF_3-Fe/N/C is much higher than that of Fe/N/C, indicating that the adsorption capacity of O_2 increases significantly. The increased oxophilic of Fe/N/C catalyst due to the introduction of CeF_3 was further verified by the MS spectra of carbon monoxide (Fig. S11). Hence, the existence of Ce^{3+} sites could remarkably enhance the O_2 adsorption capability and improve the oxophilic of Fe/N/C.

3.2. Electrochemical characterization of catalysts

The electrocatalytic performance of the catalysts was performed in RDE with 0.5 M H_2SO_4. Fig. S12 shows the CeF_3 effect on the performance of ORR, and the optimal proportion of cerium fluoride determined by electrochemical tests is 5% (the LSV curves parameters are listed in Table S3). The cyclic voltammetry (CV) curves in Fig. S13 show a wide and weak redox peak for Fe/N/C and CeF_3-Fe/N/C due to the Fe^{2+}/Fe^{3+} oxidation/reduction reaction [46]. Linear sweep voltammetry (LSV) measurements were carried out in an O_2-saturated 0.5 M H_2SO_4 solution at the rotation speed

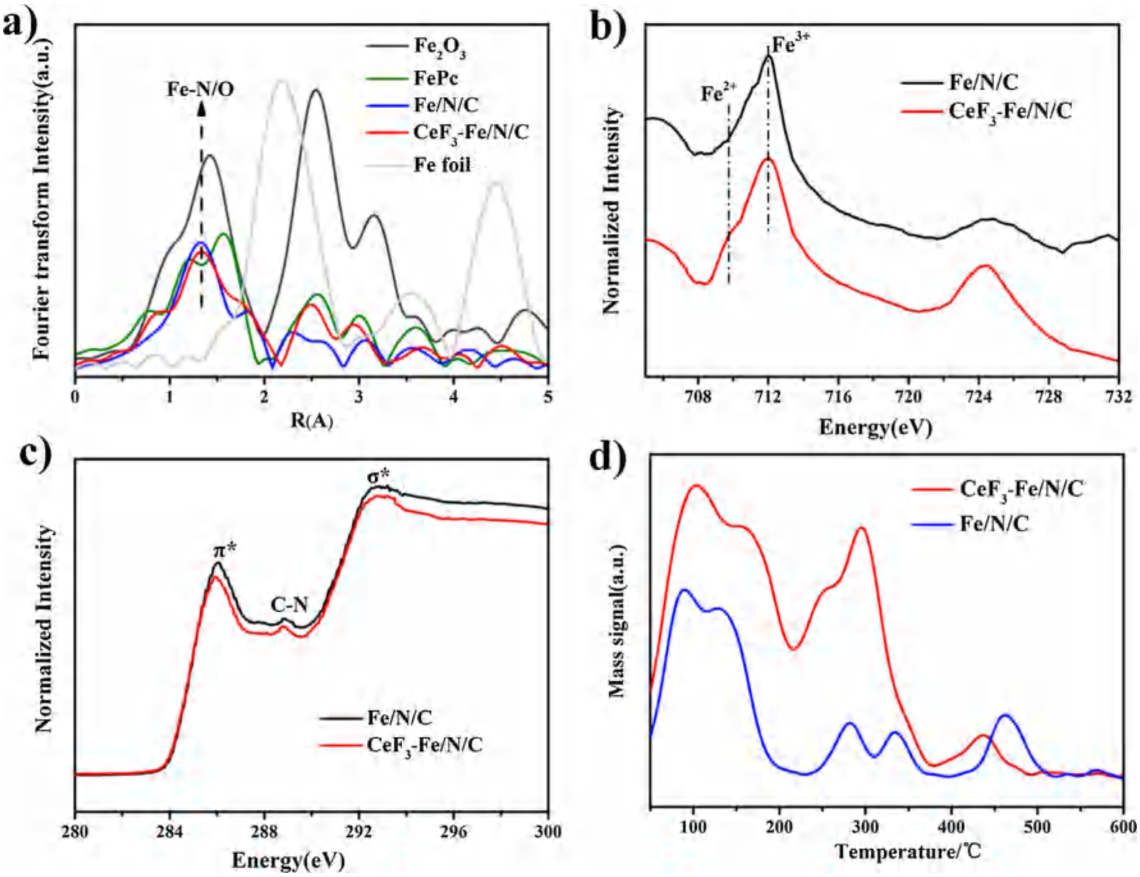

Fig. 3. (a) Fourier transformed K-edge EXAFS spectrum of iron for Fe/N/C and CeF_3-Fe/N/C. (b). Fe *L*-edge XANES spectrum of Fe/N/C and CeF_3-Fe/N/C. (c) C *K*-edge XANES spectrum of Fe/N/C and CeF_3-Fe/N/C. (d) O_2-TPD/MS profiles of Fe/N/C and CeF_3-Fe/N/C reveal the involvement of oxygen in the desorbed species.

of 1600 rmp (Fig. S14). The CeF_3-Fe/N/C and Fe/N/C show the same onset potential (0.88 V) for ORR, indicating the same intrinsic catalytic activity. This potential is 50 mV less than the value for Pt/C catalyst (0.93 V). The Fe/N/C and CeF_3-Fe/N/C exhibit the same half-wave potentials ($E_{1/2}$) of 0.78 V, only 50 mV lower than that of the commercial Pt/C. This result attributes to the high spin Fe^{3+}-N_4 configuration in the nitrogen-doped carbon as the active site responsible for the high ORR activity [37]. At a scan rate of 5 mV s^{-1}, the LSV curves of CeF_3-Fe/N/C (Fig. 4a) and Fe/N/C (Fig. 4b) at various rotation rates are tested. With the increasing of rotation rate, almost no change in onset potential is observed but current density improves due to the increased of mass transfer. Here, the Koutecky–Levich (K–L) equation is utilized to evaluate the ORR kinetics, and the K-L plots derived from RDE curves are presented in Fig. 4c and d. The average electron transfer number (n) of the CeF_3-Fe/N/C hybrid catalyst (Fig. 4c) is 3.92 (0.3 to 0.55 V versus RHE), which is significantly increased compared with the Fe/N/C (n = 3.48), suggesting the oxophilic interface between CeF_3 and Fe/N/C have a positive impact on the ORR kinetic process. As an important intermediate in the ORR process, hydrogen peroxide is also detected and quantified by RRDE test (Fig. 4e). CeF_3-Fe/N/C shows a low peroxide yield of <1%, and the average number of electrons transferred is 3.98. However, a significantly higher peroxide yield (>4%) is observed on Fe/N/C, leading to a low electron transfer number of 3.93. These results suggest that Fe/N/C doped CeF_3 has a positive influence on a direct four-electron pathway. To further elucidate the role of oxophilic interface in ORR, a cyclic stability test is performed from 0.5 to 1 V at 50 mV s^{-1}, with RDE test in O_2-saturated 0.5 M H_2SO_4 electrolyte. After 3000 cycles, the half-wave potentials of CeF_3-Fe/N/C and Fe/N/C (Fig. 4f) exhibits a negative shift of ~3 mV and ~13 mV, respectively, suggesting that the CeF_3-Fe/N/C catalyst has excellent stability in acidic media.

Furthermore, we carried out an H_2-O_2 PEMFC test to evaluate the stability of the catalysts. The fuel cell assemblies constructed by the prepared catalyst (4 mg cm^{-2}) as a cathode catalyst for ORR and Pt/C (0.5 mg cm^{-2}) as an anode catalyst for H_2 oxidation. As shown in Fig. 4g, the initial maximum power density of CeF_3-Fe/N/C cathode is about 174.2 mW m^{-2}, which is slightly greater than Fe/N/C catalyst (168.6 mW m^{-2}). This result indicates that the oxophilic interface could enhance the O_2 adsorption capability, resulting in excellent activity in PEMFC. After 24 h of catalyst stability test, the peak power density of CeF_3-Fe/N/C catalyst (135 mW m^{-2}) declined by 22%, while 28% for Fe/N/C catalyst (Fig. S15). We believe the performance can be further increased by technique optimization. Fig. 4h shows the normalized durability curves of the catalysts (the actual durability curves of the catalysts were showing Fig. S16) evaluated at a cell voltage of 0.6 V, considering the balance between cell efficiency and practical power [14]. The initial current density of Fe/N/C at 0.6 V is ~ 18% higher than that of CeF_3-Fe/N/C (103 vs. 84 mA cm^{-2}). After 24 h durability test at 0.6 V, the current density of CeF_3-Fe/N/C catalyst retains 54% of its initial value, while only 41% for the Fe/N/C catalyst. These results illustrate the excellent stability of CeF_3-Fe/N/C hybrid catalyst in the PEMFC test.

The widely recognized mechanism of instability is an oxidative attack on carbon supports and metal-coordinate active sites by H_2O_2, and subsequent leaching of the metal species, leading to rapid degradation of single-atom iron catalysts in an acidic electrolyte. As described above, investigation of the dynamic

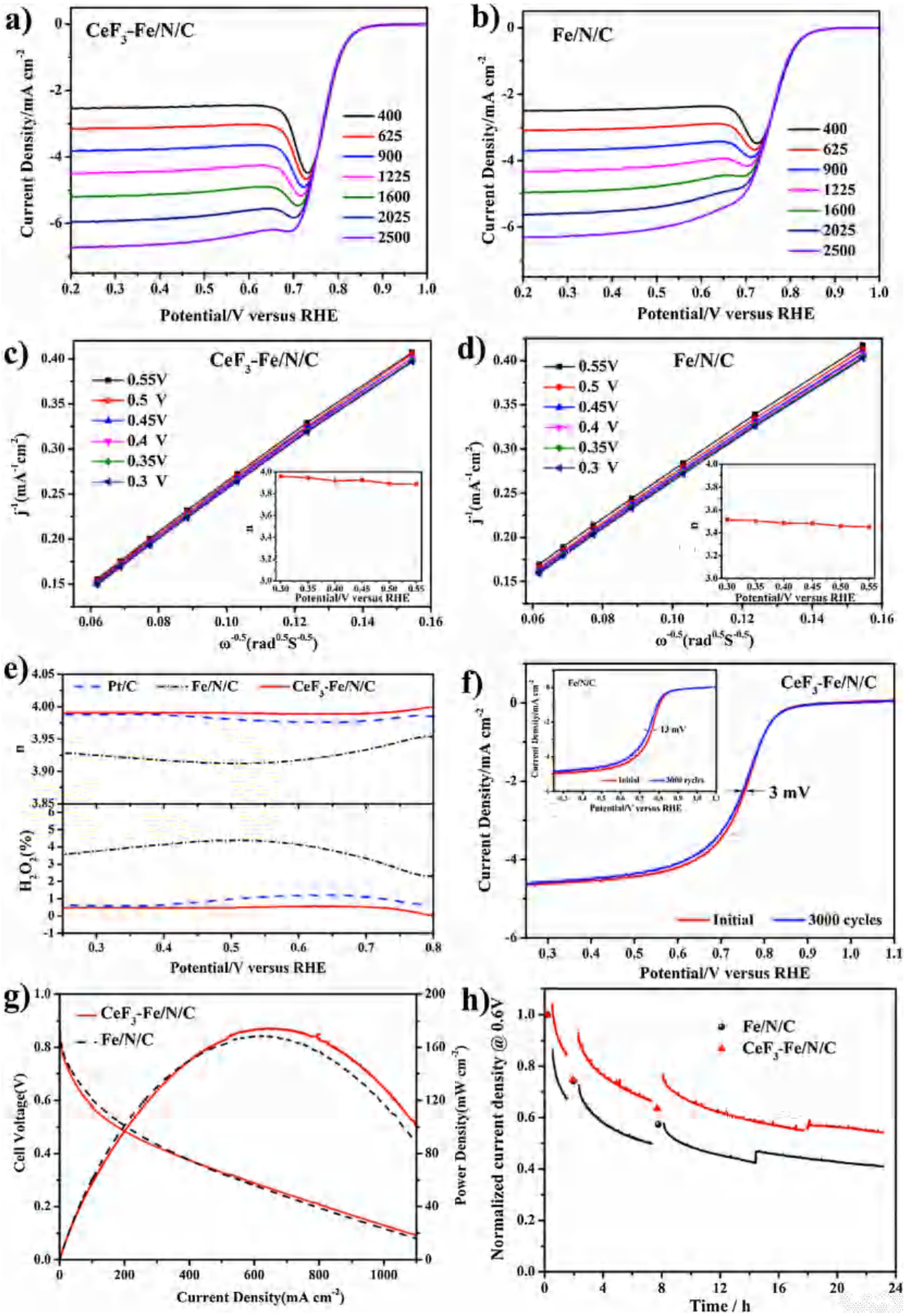

Fig. 4. LSV curves at various rotation rates in O_2-saturated 0.5 M H_2SO_4 at a scan rate of 5 mV s^{-1} for (a) CeF_3-Fe/N/C and (b) Fe/N/C. The K-L plots derived from LSV curves at various rotation rates for (c) CeF_3-Fe/N/C and (d) Fe/N/C. (e) Hydrogen peroxide yields and the electron transfer numbers of Fe/N/C and CeF_3-Fe/N/C based on the RRDE. (f) LSV curves of Fe/N/C and CeF_3-Fe/N/C before and after 3000 cycles in O_2-saturated 0.5 M H_2SO_4 solution (1600 rpm, 5 mV s^{-1}). (g) Polarization curves and power density for H_2/O_2 PEMFC at 80 °C of CeF_3-Fe/N/C and Fe/N/C. (h) The normalized stability curves of CeF_3-Fe/N/C and Fe/N/C.

production and consumption of hydrogen peroxide on atomically dispersed Fe/N/C catalyst is important [15]. Therefore, degradation of the H_2O_2-induced catalysts were investigated by an ex situ H_2O_2 treatment. The Fe/N/C and CeF_3-Fe/N/C catalysts were exposed to 10^{-3} M H_2O_2 for 24 h at 80 °C, respectively. The ORR activities of the catalysts before and after H_2O_2 treatment are presented in Fig. 5a. For both catalysts, the RDE test initial activity at 0.85 V showed a negative shift after the treatment, while the diffusion-

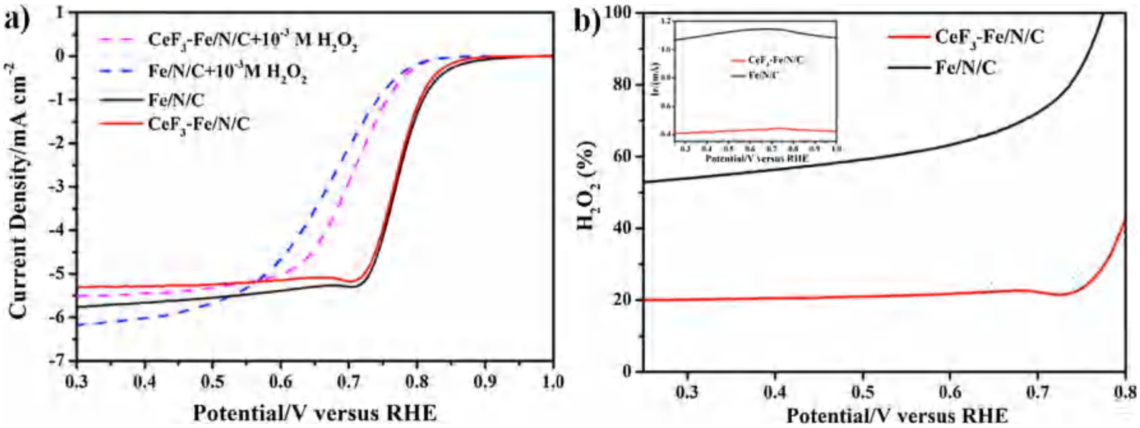

Fig. 5. (a) ORR polarization curves of Fe/N/C and CeF_3-Fe/N/C before and after H_2O_2 treatment. (b) Ring currents and the H_2O_2 yields of Fe/N/C and CeF_3-Fe/N/C in O_2-saturated 0.5 M H_2SO_4 + 5 mM H_2O_2.

limited current density does not change significantly. The result implies that the ORR mechanism is unchanged, whereas the number of active sites on the catalyst surface reduced. Owing to the higher amounts of H_2O_2, half-wave potential degradation of Fe/N/C and CeF_3-Fe/N/C were observed at 103 mV and 64 mV, respectively. Compared with Fe/N/C, the decrease of the ORR activity after H_2O_2 treatment is much larger than the CeF_3-Fe/N/C catalyst, which may be due to the restricted surface oxidation with H_2O_2. The active sites buried in the carbon layer are exposed to the electrolyte, while the Ce^{3+} sites in the CeF_3-Fe/N/C catalyst can effectively block the attack of H_2O_2 [47,48]. Furthermore, we employed H_2O_2 as a probe to investigate the hydrogen peroxide oxidation and reduction reactions in 0.5 M H_2SO_4 + 5 mM H_2O_2 catalyzed by Fe/N/C and CeF_3-Fe/N/C (Fig. 5b). The ring current of hydrogen peroxide reduction catalyzed by Fe/N/C is much higher than that of the CeF_3-Fe/N/C using RRDE test, which means that H_2O_2 can be reduced immediately and efficiently due to the high adsorption efficiency of H_2O_2 on the surface of CeF_3-Fe/N/C. The H_2O_2 yield of Fe/N/C is about 60% in the potential window of 0.25 V–0.7 V, which is much higher than that of CeF_3-Fe/N/C (20%). The yield of H_2O_2 depends on competition between desorption and reduction of H_2O_2 on the surface of the catalyst, which is determined by the surface state of catalysts [16,48]. Thus, the Ce^{3+} sites of CeF_3-Fe/N/C can absorb and convert H_2O_2 into water effectively. As a result, the attack of H_2O_2 can be relieved, achieving much better stability than Fe/N/C catalyst in an acidic electrolyte.

4. Conclusions

In summary, we reported a bottom-up strategy to synthesize a cerium fluoride/single-atom dispersed Fe/N/C hybrid catalyst using fluoride agent and NH_3 activation, as well as the oxophilic interfaces was formed between atomically dispersed iron-nitrogen-carbon and CeF_3. By dispersing CeF_3 on the surface of Fe/N/C, the surface chemical state redistribution could occur at the interface. We demonstrated that the CeF_3-Fe/N/C catalyst can achieve excellent electrochemical performance and superior durability in PEMFC. The presence of Ce^{3+} sites can promote O_2 adsorption and reduce of H_2O_2 into the water effectively. Thus, the potential adverse effects caused by low-concentration oxygen reacts with active sites in the catalysts, and H_2O_2 attack during ORR in the cathode are eliminated. Engineering of a nanostructured interface between the metal fluoride/single iron atom hybrid catalyst opens a new way to enhance the performance of the noble-metal-free catalyst in PEMFC.

Acknowledgment

This work was supported by the Nature Science Foundation of China (No. 21575015, 21203008), the Beijing Nature Science Foundation (No. 2172051), the National Key Research and Development Program of China "New Energy Project for Electric Vehicle" (2016YFB0100204). Thanks for Dr. Lirong Zheng (1W1B@Beijing Synchrotron Radiation Facility) for providing measurement time. We appreciate help from Dr. Shuhu Liu (4B7B@Beijing Synchrotron Radiation Facility) for XAS measurement. We thank Prof. Shaorui Sun (Beijing University of Technology) and Prof. Ligang Feng (Yangzhou University) for useful discussion. XRD measurements were performed in the Analysis & Testing Center, Beijing Institute of Technology.

Appendix A. Supplementary material

Supplementary data to this article can be found online at https://doi.org/10.1016/j.jcat.2019.04.028.

References

[1] M.E. Scofield, H. Liu, S.S. Wong, A concise guide to sustainable PEMFCs: recent advances in improving both oxygen reduction catalysts and proton exchange membranes, Chem. Soc. Rev. 44 (2015) 5836–5860.
[2] Y.J. Wang, N.N. Zhao, B.Z. Fang, H.T. Li, X.T. Bi, H.J. Wang, Carbon-supported Pt-based alloy electrocatalysts for the oxygen reduction reaction in polymer electrolyte membrane fuel cells: particle size, shape, and composition manipulation and their impact to activity, Chem. Rev. 115 (2015) 3433–3467.
[3] Y. Nie, L. Li, Z.D. Wei, Recent advancements in Pt and Pt-free catalysts for oxygen reduction reaction, Chem. Soc. Rev. 44 (2015) 2168–2201.
[4] N.R. Sahraie, U.I. Kramm, J. Steinberg, Y.J. Zhang, A. Thomas, T. Reier, J.P. Paraknowitsch, P. Strasser, Quantifying the density and utilization of active sites in non-precious metal oxygen electroreduction catalysts, Nat. Common. 6 (2015) 8618.
[5] J.K. Li, S. Ghoshal, W.T. Liang, M.T. Sougrati, F. Jaouen, B. Halevi, S. McKinney, G. McCool, C.R. Ma, X. Yuan, Z.F. Ma, S. Mukerjee, Q.Y. Jia, Structural and mechanistic basis for the high activity of Fe–N–C catalysts toward oxygen reduction, Energy Environ. Sci. 9 (2016) 2418–2432.
[6] Y.J. Chen, S.F. Ji, Y.G. Wang, J.C. Dong, W.X. Chen, Z. Li, R.G. Shen, L.R. Zheng, Z.B. Zhuang, D.S. Wang, Y.D. Li, Isolated single iron atoms anchored on N-doped porous carbon as an efficient electrocatalyst for the oxygen reduction reaction, Angew. Chem. Int. Ed. 24 (2017) 7041–7045.
[7] A. Zitolo, V. Goellner, V. Armel, M.T. Sougrati, T. Mineva, L. Stievano, E. Fonda, F. Jaouen, Identification of catalytic sites for oxygen reduction in iron-and nitrogen-doped graphene materials, Nat. Mater. 14 (2015) 937–942.
[8] J. Wang, Z.Q. Huang, W. Liu, C.R. Chang, H.L. Tang, Z.J. Li, W.X. Chen, C.J. Jia, T. Yao, S.Q. Wei, Y.E. Wu, Y.D. Li, Design of N-coordinated dual-metal sites: a stable and active Pt-free catalyst for acidic oxygen reduction reaction, J. Am. Chem. Soc. 139 (2017) 17281–17284.
[9] Z.Y. Lu, W.W. Xu, J. Ma, Y.J. Li, X.M. Sun, L. Jiang, Superaerophilic carbon-nanotube-array electrode for high-performance oxygen reduction reaction, Adv. Mater. 28 (2016) 7155–7161.

[10] J.K. Nørskov, J. Rossmeisl, A. Logadottir, L. Lindqvist, J.R. Kitchin, T. Bligaard, H. Jonsson, Origin of the overpotential for oxygen reduction at a fuel-cell cathode, J. Phys. Chem. B 108 (2004) 17886–17892.

[11] L. Lv, D. Zha, Y. Ruan, Z. Li, X. Ao, J. Zheng, J. Jiang, H.M. Chen, W.H. Chiang, J. Chen, C.D. Wang, A universal method to engineer metal oxide–metal–carbon interface for highly efficient oxygen reduction, ACS Nano 12 (2018) 3042–3051.

[12] M. Qiao, C. Tang, L.C. Tanase, C.M. Teodorescu, C. Chen, Q. Zhang, M.M. Titirici, Oxygenophilic ionic liquids promote the oxygen reduction reaction in Pt-free carbon electrocatalysts, Mater. Horiz. 4 (2017) 895–899.

[13] D. Banham, S. Ye, K. Pei, J.I. Ozaki, T. Kishimoto, Y. Imashiro, A review of the stability and durability of non-precious metal catalysts for the oxygen reduction reaction in proton exchange membrane fuel cells, J. Power Sources 285 (2015) 334–348.

[14] G.X. Zhang, R. Chenitz, M. Lefèvre, S.H. Sun, J.P. Dodelet, Is iron involved in the lack of stability of Fe/N/C electrocatalysts used to reduce oxygen at the cathode of PEM fuel cells?, Nano Energy 29 (2016) 111–125

[15] V. Goellner, V. Armel, A. Zitolo, E. Fonda, F. Jaouen, Degradation by hydrogen peroxide of metal-nitrogen-carbon catalysts for oxygen reduction, J. Electrochem. Soc. 162 (2015) 403–414.

[16] X.H. Zhang, P. Lu, C. Zhang, X.Z. Cui, Y.F. Xu, H.Y. Qu, J. Shi, Towards understanding ORR activity and electron-transfer pathway of MN_x/C electrocatalyst in acidic media, J. Catal. 356 (2017) 229–236.

[17] S. Phokha, S. Hunpratub, B. Usher, A. Pimsawat, N. Chanlek, S. Maensiri, Effects of CeO_2, nanoparticles on electrochemical properties of carbon/CeO_2 composites, Appl. Surf. Sci. 446 (2018) 36–46.

[18] Y. Yu, X.F. Wang, W.Y. Gao, P. Li, W. Yan, S. Wu, Q.H. Cui, W. Song, K.J. Ding, Trivalent cerium-preponderant CeO_2/graphene sandwich-structured nanocomposite with greatly enhanced catalytic activity for the oxygen reduction reaction, J. Mater. Chem. A 5 (2017) 6656–6663.

[19] W. Xia, J.J. Li, T. Wang, L. Song, H. Guo, H. Gong, C. Jiang, B. Gao, J.P. He, The synergistic effect of Ceria and Co in N-doped leaf-like carbon nanosheets derived from a 2D MOF and their enhanced performance in the oxygen reduction reaction, Chem. Commun. 54 (2018) 1623–1626.

[20] P.F. Ji, L.Z. Wang, F. Chen, J.L. Zhang, Ce^{3+}-centric organic pollutant elimination by CeO_2 in the presence of H_2O_2, ChemCatChem 2 (2010) 1552–1554.

[21] T.S. Wu, Y.Y. Zhou, R.F. Sabirianov, W.N. Mei, Y.L. Soo, C.L. Cheung, X-ray absorption study of ceria nanorods promoting the disproportionation of hydrogen peroxide, Chem. Commun. 52 (2016) 5003–5006.

[22] H. Wei, X. Su, J. Liu, J. Tian, Z. Wang, K. Sun, Z. Rui, W. Yang, Z.G. Zou, A CeO_2 modified phenylenediamine-based Fe/N/C with enhanced durability/stability as non-precious metal catalyst for oxygen reduction reaction, Electrochem. Commun. 88 (2018) 19–23.

[23] L. Yang, Z. Cai, L. Hao, Z.P. Xing, Y. Dai, X. Xu, S. Pan, Y.Q. Duan, J.L. Zou, Nano Ce_2O_2S with highly enriched oxygen-deficient Ce^{3+} sites supported by N and S dual-doped carbon as an active oxygen-supply catalyst for the oxygen reduction reaction, ACS Appl. Mater. Interfaces 9 (2017) 22518–22529.

[24] N.P. Deng, J.G. Ju, J. Yan, X.H. Zhou, Q.Q. Qin, K. Zhang, Y. Liang, Q.X. Li, W.M. Kang, B.W. Cheng, CeF_3-doped porous carbon nanofibers as sulfur immobilizers in cathode material for high-performance lithium–sulfur batteries, ACS Appl. Mater. Interfaces 10 (2018) 12626–12638.

[25] H. Zhou, L. Zhang, S. Gao, H. Liu, L. Xu, X.H. Wang, M. Yan, Hydrogen storage properties of activated carbon confined $LiBH_4$ doped with CeF_3 as catalyst, Int. J. Hydrogen Energy 42 (2017) 23010–23017.

[26] Y. Xiang, B.R. Cheng, D.F. Li, B.X. Zhou, T.F. Yang, S.S. Ding, G.F. Huang, A. Pan, W.Q. Huang, Facile one-step in-situ synthesis of type-II CeO_2/CeF_3 composite with tunable morphology and photocatalytic activity, Ceram. Int. 42 (2016) 16374–16381.

[27] V.V. Pavlov, R.M. Rakhmatullin, O.A. Morozov, S.L. Korableva, A.G. Kiiamov, A. K. Naumov, V.V. Semashko, V.G. Evtugyn, Y.N. Osin, CeO_2/CeF_3 composite nanoparticles: fabrication by fluorination of CeO_2 with tetrafluoromethane gas, Mater. Chem. Phys. 207 (2018) 542–546.

[28] Y.G. Wang, C.C. Yin, H.F. Qin, Y.Z. Wang, Y.G. Li, X. Li, Y. Zuo, S. Kang, L. Cui, A urea-assisted template method to synthesize mesoporous N-doped CeO_2 for CO_2 capture, Dalton Trans. 44 (2015) 18718–18722.

[29] Y. Yu, L. Gao, X.C. Liu, Y.H. Wang, S.X. Xing, Enhancing the catalytic activity of zeolitic imidazolate framework-8-derived N-doped carbon with incorporated CeO_2 nanoparticles in the oxygen reduction reaction, Chem. Eur. J. 23 (2017) 10690–10697.

[30] J. Chun, C. Jo, S. Sahgong, M.G. Kim, E. Lim, D.H. Kim, J. Hwang, E. Kang, K.A. Ryu, Y.S. Jung, Y. Kim, J. Lee, Ammonium fluoride mediated synthesis of anhydrous metal fluoride–mesoporous carbon nanocomposites for high-performance lithium ion battery cathodes, ACS Appl. Mater. Interfaces 51 (2016) 35180–35190.

[31] P.W. Yu, R.J. Chen, Q. Zhang, S.H. Liang, M. Ni, W. Yang, Porous carbon supported atomic iron as electrocatalysts for acidic oxygen reduction reaction, Sci. Bull. 63 (2018) 213–215.

[32] I. Moog, C. Prestipino, S. Figueroa, J. Majimel, A. Demourgues, Dual Ce^{4+}/Fe^{3+} redox phenomena into nanocrystalline $Ce_{1-x}Fe_xO_{2-x/2}$ solid solution, J. Phys. Chem. C 118 (2014) 22746–22753.

[33] J.M. Luo, X.L. Tian, J.H. Zeng, Y.W. Li, H.Y. Song, S.J. Liao, Limitations and improvement strategies for early-transition-metal nitrides as competitive catalysts toward the oxygen reduction reaction, ACS Catal. 6 (2016) 6165–6174.

[34] C. Giordano, A. Kraupner, I. Fleischer, C. Henrich, G. Klingelhöfer, M. Antonietti, Non-conventional Fe_3C-based nanostructures, J. Mater. Chem. 21 (2011) 16963–16967.

[35] J. Zhou, P.N. Duchesne, Y. Hu, J. Wang, P. Zhang, Y. Li, T. Regier, H.J. Dai, Fe–N bonding in a carbon nanotube–graphene complex for oxygen reduction: an XAS study, Phys. Chem. Chem. Phys. 16 (2014) 15787–15791.

[36] H. Zhang, S. Hwang, M. Wang, Z.X. Feng, S. Karakalos, L. Luo, Z. Qiao, X. Xie, C. Wang, D. Su, Y. Shao, G. Wu, Single atomic iron catalysts for oxygen reduction in acidic media: particle size control and thermal activation, J. Am. Chem. Soc. 139 (2017) 14143–14149.

[37] M. Xiao, J.B. Zhu, L. Ma, Z. Jin, J.J. Ge, X. Deng, Y. Hou, Q.G. He, J.K. Li, Q.Y. Jia, S. Mukerjee, R. Yang, Z. Jiang, D. Su, C.P. Liu, W. Xing, Microporous framework induced synthesis of single-atom dispersed Fe-N-C acidic ORR catalyst and its in situ reduced Fe-N_4 active site identification revealed by X-ray absorption spectroscopy, ACS Catal. 8 (2018) 2824–2832.

[38] U.I. Kramm, M. Lefèvre, N. Larouche, D. Schmeisser, J.P. Dodelet, Correlations between mass activity and physicochemical properties of Fe/N/C catalysts for the ORR in PEM fuel cell via ^{57}Fe Mossbauer spectroscopy and other techniques, J. Am. Chem. Soc. 3 (2014) 978–985.

[39] Y. Han, Y.G. Wang, R.R. Xu, W.X. Chen, L.R. Zheng, A.J. Han, Y. Zhu, J. Zhang, H.B. Zhang, J. Luo, C. Chen, Q. Peng, D.S. Wang, Y.D. Li, Electronic structure engineering to boost oxygen reduction activity by controlling the coordination of the central metal, Energy Environ. Sci. 11 (2018) 2348–2352.

[40] Q.Q. Cheng, L.J. Yang, L.L. Zou, Z.Q. Zou, C. Chen, Z. Hu, H. Yang, Single cobalt atom and N codoped carbon nanofibers as highly durable electrocatalyst for oxygen reduction reaction, ACS Catal. 7 (2017) 6864–6871.

[41] J. Melke, B. Peter, A. Habereder, J. Ziegler, C. Fasel, A. Nefedov, H. Sezen, C. Wöll, H. Ehrenberg, C. Roth, Metal–support interactions of platinum nanoparticles decorated N-doped carbon nanofibers for the oxygen reduction reaction, ACS Appl. Mater. Interfaces 8 (2016) 82–90.

[42] D.S. Geng, S.L. Yang, Y. Zhang, J.L. Yang, J. Liu, R.Y. Li, T.K. Sham, X.L. Sun, S. Ye, S. Knights, Nitrogen doping effects on the structure of graphene, Appl. Surf. Sci. 257 (2011) 9193–9198.

[43] T. Masuda, H. Fukumitsu, K. Fugane, H. Togasaki, D. Matsumura, K. Tamura, Y. Nishihata, H. Yoshikawa, K. Kobayashi, T. Mori, K. Uosaki, Role of cerium oxide in the enhancement of activity for the oxygen reduction reaction at Pt-CeO_x nanocomposite electrocatalyst-an in situ electrochemical X-ray absorption fine structure study, J. Phys. Chem. C 116 (2012) 10098–10102.

[44] Y. Zheng, K.Z. Li, H. Wang, D. Tian, Y.H. Wang, X. Zhu, Y.G. Wei, M. Zheng, Y.M. Luo, Designed oxygen carriers from macroporous $LaFeO_3$ supported CeO_2 for chemical-looping reforming of methane, Appl. Catal. B: Environ. 202 (2017) 51–63.

[45] Y.T. Meng, W.Q. Song, H. Huang, Z. Ren, S.Y. Chen, S.L. Suib, Structure–property relationship of bifunctional MnO_2 nanostructures: highly efficient, ultra-stable electrochemical water oxidation and oxygen reduction reaction catalysts identified in alkaline media, J. Am. Chem. Soc. 136 (2014) 11452–11464.

[46] S.H. Liang, R.J. Chen, P.W. Yu, M. Ni, Q. Zhang, X.L. Zhang, W. Yang, Ionically dispersed Fe (II)–N and Zn (II)–N in porous carbon for acidic oxygen reduction reactions, Chem. Commun. 53 (2017) 11453–11456.

[47] D. Damatov, J.M. Mayer, (Hydro) peroxide ligands on colloidal cerium oxide nanoparticles, Chem. Commun. 52 (2016) 10281–10284.

[48] I. Katsounaros, W.B. Schneider, J.C. Meier, U. Benedikt, P.U. Biedermann, A. Cuesta, The impact of spectator species on the interaction of H_2O_2 with platinum–implications for the oxygen reduction reaction pathways, Phys. Chem. Chem. Phys. 15 (2013) 8058–8068.